J. Fluid Mech. (1996), vol. 321, pp. 121–136

Thermal convection in a magnetic fluid

By ABDELFATTAH ZEBIB

Department of Mechanical and Aerospace Engineering, Rutgers University, Piscataway, NJ 08855, USA

(Received 17 January 1996 and in revised form 18 March 1996)

A theoretical study of the character and stability of thermomagnetic flow in a microgravity environment is performed. Convection is driven owing to imposed radial magnetic and temperature gradients in a cylindrical shell containing a ferrofluid. Linear, nonlinear, and computational methods are employed. It is shown that convection sets in as a stable supercritical bifurcation. Results obtained for a specific shell configuration are in good agreement with experiments.

1. Introduction

Natural convective motions occur on Earth owing to density variation with temperature in the gravitational body force field. This, of course, has important practical applications in many processes involving thermal management. In the microgravity environment of space this free convection ceases to exist. An alternative may be provided by the use of magnetic fluids and manipulating existing magnetic fields. These ferrofluids are colloidal suspensions of magnetic particles, about 10 nm, in ordinary fluids such as water, kerosene, or organic liquids. A surfactant coating is used to prevent coalescence of the particles (Rosensweig 1985, 1987). Commercial production of these magnetic fluids has resulted in their use in a number of engineering applications (Berkovsky, Vedvedev & Krakov 1993). The magnetic particles are influenced by thermal Brownian motion and in the absence of a magnetic field the net magnetization is zero. An external magnetic field of intensity $\boldsymbol{H}$ will tend to align the dipole moments of the particles. Thus a net magnetization $\boldsymbol{M}$ develops and is a decreasing function of temperature. If, in addition, the applied magnetic field is non-uniform in space, a force $\mu_0 \boldsymbol{M} \nabla \boldsymbol{H}$ (μ_0 is the permeability of free space) will act on the fluid in the direction of increasing field. In the presence of a temperature gradient the variation of $\boldsymbol{M}$ can induce fluid motion (analogous to density variation in buoyant convection). If ∇T is parallel to $\nabla \boldsymbol{H}$ then a situation of thermal instability develops similar to the Rayleigh–Bénard problem. Thermomagnetic instability in a fluid layer heated from below was considered by Finlayson (1970). More recently, Stiles & Blennerhassett (1993) determined the influence of a radial temperature gradient on Couette flow of a ferrofluid.

The present paper is concerned with an internally heated cylindrical shell. A radial magnetic field is produced by an electric current through the cylinder axis. Polevikov & Fertman (1977) used a finite-difference method to compute buoyant-magnetic convection. They only considered two-dimensional azimuthal states and established critical conditions for transition from extrapolation to zero motion. Odenbach (1993) carried out a drop tower experiment with a shell of aspect ratio 0.46. His temperature measurements of nonlinear convection indicated a motion with 4 counter-rotating azimuthal cells and his extrapolated value for the critical magnetic Rayleigh number

agreed well with that computed by Polevikov & Fertman (1977). In this paper we present a reasonably complete study of the problem. Linear stability methods are used to determine critical states. Asymptotic methods are then employed to establish the stable supercritical nature of the bifurcations. We show that onset of convection in Odenbach's cylinder is indeed three-dimensional. We carry out direct numerical simulations using finite-volumes to study the resulting motions. This is followed by numerical experiments with a variety of initial conditions from which we conclude that the azimuthal motion observed by Odenbach regains stability and is the preferred form of convection at increasing nonlinearity.

2. Mathematical model

The motion is described in a cylindrical coordinate system (r, θ, z). We consider an incompressible fluid-filled infinitely long cylindrical shell of inner and outer radii R_1 and R_2, with the aspect ratio $\eta = R_1/R_2 < 1$. The inner and outer cylindrical surfaces are isothermal at temperatures T_1 and T_2 $(\Delta T = T_1 - T_2 > 0)$, respectively. An azimuthal magnetic field with intensity $H_0(r)$, is generated owing to an electric current I along the inner cylinder according to:

$$H_0 = \frac{I}{2\pi r}. \tag{1}$$

The formulation of the equilibrium continuum model described in Bashtovoy, Berkovsky & Vislovich (1988) is adopted. It is assumed that the magnetic field intensity $\boldsymbol{H}$ and magnetization $\boldsymbol{M}$ are parallel with $\boldsymbol{M} = (M/H)\boldsymbol{H}$, and M determined by an equation of state $M(T, \rho, H)$. The magnetic fluid is assumed to retain its Newtonian character with an additional Maxwellian stress tensor $-\mu_0(H^2/2)\delta_{ij} + H_i B_j$, where the magnetic induction $\boldsymbol{B} = \mu_0(\boldsymbol{M} + \boldsymbol{H})$. Maxwell's equations require that $\nabla \cdot \boldsymbol{B} = 0$, and for a non-conducting medium $\nabla \times \boldsymbol{H} = 0$. The non-inductive approximation is adopted so that the field intensity remains as given in (1). A linear magnetic equation of state is taken according to:

$$M = M_0 - K(T - T_0), \tag{2}$$

where K is the pyromagnetic coefficient, and subscript 0 denotes equilibrium reference values. We scale the Navier–Stokes equations using $d = R_2 - R_1$, κ/d, d^2/κ, ΔT, $\mu\kappa/d^2$ for length, velocity, time, temperature, and pressure, respectively, where, κ is the thermal diffusivity, and μ is the dynamic viscosity. With all thermodynamic properties assumed constant, the non-dimensional equations of motion, with zero gravitational force as appropriate to a microgravity environment, are:

$$\nabla \cdot \boldsymbol{V} = 0, \tag{3a}$$

$$\frac{1}{Pr}\left\{\frac{\partial \boldsymbol{V}}{\partial t} + \nabla \cdot (\boldsymbol{V}\boldsymbol{V})\right\} = -\nabla p + \nabla^2 \boldsymbol{V} + \frac{R_m}{r^2} r_1 r_2 T \boldsymbol{e}_r, \tag{3b}$$

$$\frac{\partial T}{\partial t} + \nabla \cdot (\boldsymbol{V}T) = \nabla^2 T. \tag{3c}$$

In (3) r_1 and $r_2 = r_1 + 1$ are the non-dimensional radii $((R_1/d) = \eta/(1-\eta)$, $R_2/d = 1/(1-\eta)$, respectively), and the magnetic Rayleigh number $R_m = \mu_0 KG\Delta T d^3/\rho\kappa\nu$. G is the magnetic gradient $\Delta H_0/d$, where ΔH_0 is the drop in H_0 across the

fluid layer, ν is the kinematic viscosity, the Prandtl number $Pr = \nu/\kappa$, and $\boldsymbol{e}_r$ is a unit radical vector. It is seen that the role played by the magnetic field is similar to that of buoyancy in a Boussenisq fluid (e.g. Busse & Riahi 1982). The boundary conditions associated with (3) are:

$$V = 0 \quad \text{on } r = r_1 \text{ and } r_2, \tag{4a}$$

$$T = 1 \quad \text{on } r = r_1, \tag{4b}$$

$$T = 0 \quad \text{on } r = r_2. \tag{4c}$$

3. Linear stability

The system (3) and (4) admits the conduction solution:

$$V = 0, \tag{5a}$$

$$T = T_c = \ln(r/r_2)/\ln\eta. \tag{5b}$$

This solution, however, can become unstable and convection initiated if the strength of the applied magnetic field, or the applied temperature difference increases, or simply at some critical value of R_m. A linear stability analysis can be performed by assuming disturbances to the solution in (5) of the form $\{p, V_r, V_\theta, V_z, \Theta\}(r)\exp\{\sigma t + in\theta + ikz\}$, where n and k are azimuthal and axial wavenumbers, respectively. The resulting linearized equations are:

$$\mathrm{D}^* V_r + \frac{in}{r} V_\theta + ikV_z = 0, \tag{6a}$$

$$\frac{\sigma}{Pr} V_r = -\mathrm{D}p + \left[\mathrm{DD}^* - k^2 - \frac{n^2}{r^2}\right] V_r - \frac{2in}{r^2} V_\theta + \frac{R_m r_1 r_2}{r^2}\Theta, \tag{6b}$$

$$\frac{\sigma}{Pr} V_\theta = -\frac{in}{r}p + \left[\mathrm{DD}^* - k^2 - \frac{n^2}{r^2}\right] V_\theta + \frac{2in}{r^2} V_r, \tag{6c}$$

$$\frac{\sigma}{Pr} V_z = -ikp + \left[\mathrm{D}^*\mathrm{D} - k^2 - \frac{n^2}{r^2}\right] V_z, \tag{6d}$$

$$\sigma\Theta = \left[\mathrm{D}^*\mathrm{D} - k^2 - \frac{n^2}{r^2}\right]\Theta - V_r T_c', \tag{6e}$$

with $\mathrm{D} = \mathrm{d}/\mathrm{d}r$, and $\mathrm{D}^* = (\mathrm{d}/\mathrm{d}r) + (1/r)$. The boundary conditions require $\{V_r, V_\theta, V_z, \Theta\} = 0$ at r_1, r_2. In addition, because of periodicity, the wavenumber n is restricted to the integers. This system defines an eigenvalue problem for $\sigma(n, k, \eta, Pr; R_m)$. Exchange of stabilities could not be shown analytically, and in general σ is expected to be complex valued.

There are three possible distinct patterns of motions. A two-dimensional azimuthal motion with $k = 0$ of the type observed by Odenbach (1993). A two-dimensional meridional motion with $n = 0$ similar to Taylor cells (Chandrasekhar 1961). Also possible is three-dimensional convection with both n and k non-zero. When $n \neq 0$, one can eliminate p and V_θ and derive an eighth-order system for V_r, V_z, and Θ with boundary conditions $\{V_r, DV_r, V_z, \Theta\} = 0$ at r_1, r_2. Likewise, when $k \neq 0$, one can

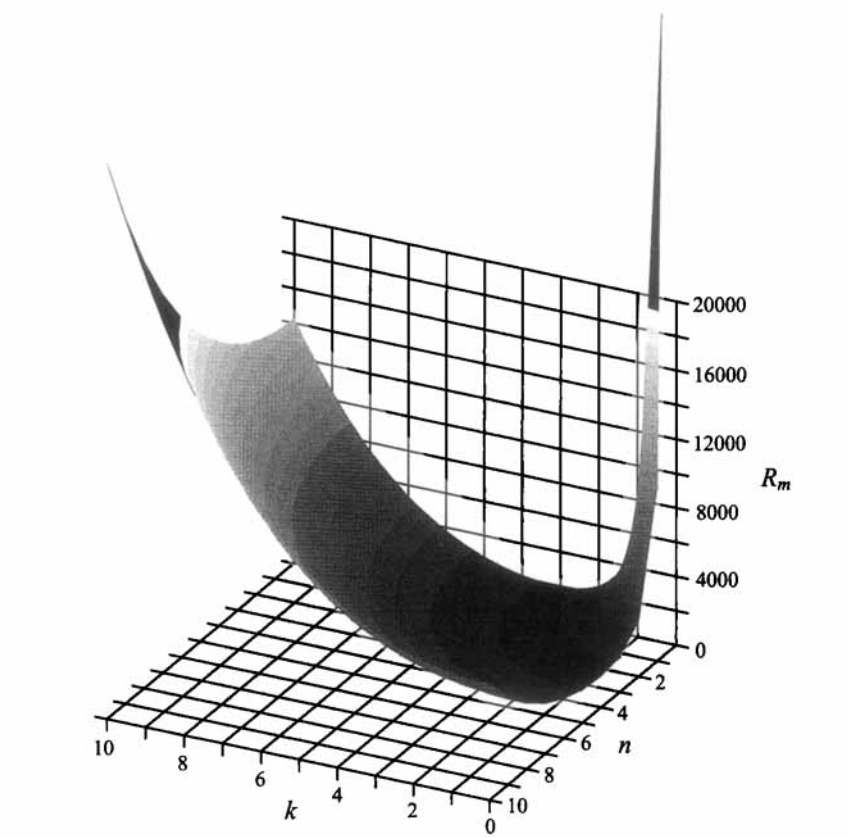

FIGURE 1. Stability surface in $n-k-R_m$ space for $\eta = 0.46$. The critical state is three-dimensional with $n = 3$, $k = 2.04$, and $R_m = 1802.36$.

eliminate p and V_z and derive an eighth-order system for V_r, V_θ, and Θ with boundary conditions $\{V_r, DV_r, V_\theta, \Theta\} = 0$ at r_1, r_2. These systems are then solved using a pseudospectral Chebyshev method (Gottlieb & Orszag 1977) with Eispack routines employed for computing the eigenvalues of the resulting generalized matrix eigenvalue problems. In addition, pseudospectral solutions of (6) without elimination of p was also accomplished (this was needed in §4 for solving the bifurcation problem of three-dimensional states). The three approaches, involving solutions of different differential systems, produced identical solutions which served as a check. It was found that all critical states computed for all values of η, n, k, and Pr are stationary with $\sigma = 0$. Thus, as evident from (6), critical conditions are independent of Pr.

For a given η, $\sigma = 0$ states define a three-dimensional surface in $n-k-R_m$ space. This surface is shown in figure 1 for $\eta = 0.46$ which corresponds to Odenbach's (1993) drop-tower experiment. The minimum R_m determines the critical state and occurs at $n = 3$, $k = 2.04$, and $R_m = 1802.36$. The value of R_m agrees well with both the experiment and the computations of Polevikov & Fertman (1977). A close-up on the critical point of figure 1 is obtained by taking cross-sections at constant values of n. The results shown in figure 2 indicate bunching of modes near $R_{m_{cr}}$. Thus, while linear theory predicts a three-dimensional onset, there are other competing states in the vicinity and nonlinear analyses and computations are necessary to further clarify the situation. We find three-dimensional onset of motion, while experiments predict an

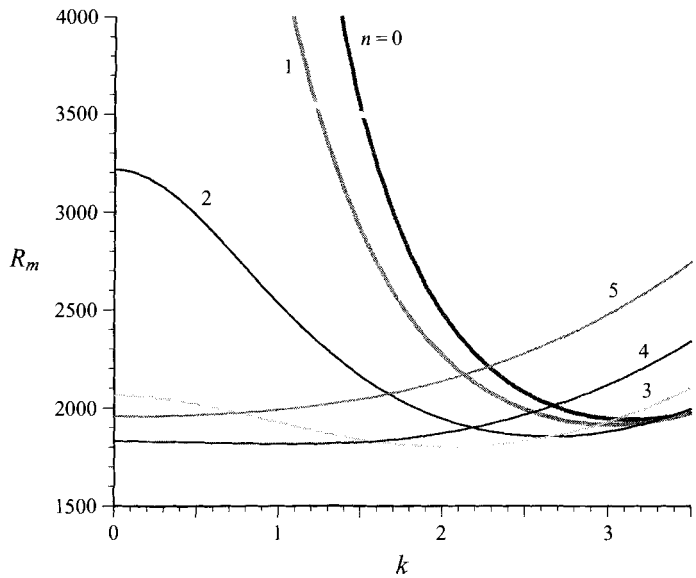

FIGURE 2. Stability curves for $\eta = 0.46$ generated from $n = 0$–5 sections of the stability surface in figure 1. Azimuthal convection occurs first with $n = 4$ and $R_m = 1831.23$, while meridional motions are possible with $k = 3.1$ and $R_m = 1940.99$.

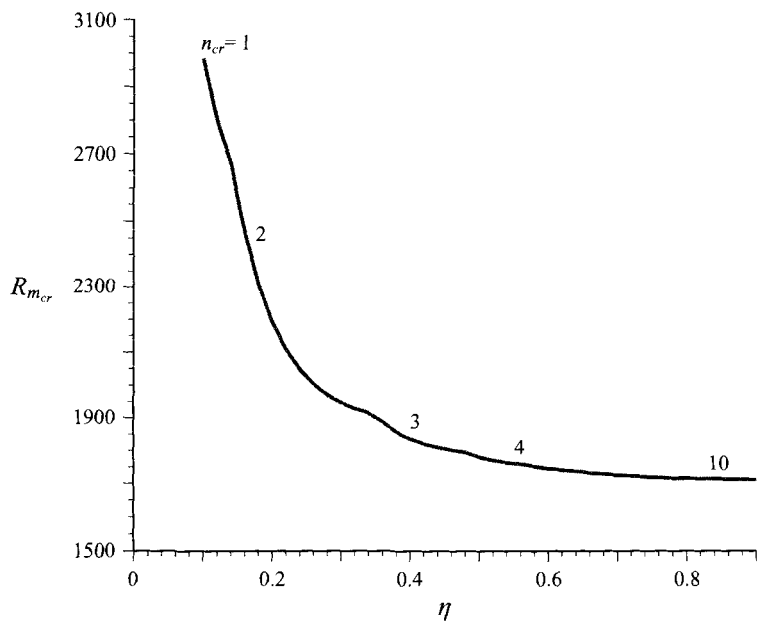

FIGURE 3. Critical R_m as function of η. There are patches of η with constant n_{cr} with k_{cr} (not shown) increasing with η on each patch. $R_{m_{cr}} \to$ the plane layer value 1707.76 as $\eta \to 1$.

$n = 4$ motion with no indication of whether it be two or three dimensional. It should be noted that the critical R_m for two-dimensional azimuthal convection with $n = 4$ and $k = 0$ is a very close 1831.23, while the lowest value for onset of meridional convection with $n = 0$ and $k = 3.1$ is a distant 1940.99. The apparent discrepancy between linear theory and experiments will be addressed by subsequent nonlinear considerations (the

axial magnetic field used in the experiments to align the convection along the axis may influence the dynamics and may contribute to this apparent discrepancy).

The influence of η on linear instability is summarized in figure 3. It is seen that $R_{m_{cr}}$ decreases with η. While n_{cr} increases with η, there are patches of η with constant n_{cr}. On these patches, k_{cr} also increases with η. As $\eta \to 1 (r_1, r_2 \to \infty)$, the governing equations (6) are transformed to those of the Bénard problem (Chandrasekhar 1961) using $\zeta = r - r_1$, $\mathrm{D} = \mathrm{D}^* = \mathrm{d}/\mathrm{d}\zeta$, $n = r_1 m$, and a total wavenumber $a^2 = m^2 + k^2$. Thus $R_{m_{cr}}$ asymptotically approaches 1707.76 as shown in figure 3. The fact that the limiting operator is self-adjoint, implies both that exchange of stabilities holds, and that stable supercritical bifurcation (Joseph 1976) is expected with $\eta = 1$. The former result is consistent with our solutions of equations (6) with $\eta \neq 1$, and the latter will be shown to also hold with $\eta \neq 1$.

4. Bifurcating solutions

Linear considerations predict a single critical state for each η. It also shows the clustering of eigensolutions and thus various nonlinear branches are expected to exist near onset. The character of nonlinear states as well as their stabilities will be determined in §5 using direct numerical solutions of equations (3) and (4). In this section we determine properties of bifurcating solutions following the asymptotic methods of Schlüter, Lortz & Busse (1965) and Busse & Riahi (1982). Because magnetic fluids have Prandtl numbers about 10 or larger, we will restrict attention to the case of infinite Pr. This simplifies the algebra, and the assumption will be seen in the next section to be accurate. First, we write equations (3) in the form (with $T = T_c + \Theta$),

$$X = \{p, V_r, V_\theta, V_z, \Theta\}^T. \tag{7a}$$

$$(\boldsymbol{L} + R_m \boldsymbol{M}) X = N(X, X), \tag{7b}$$

where, with primes denoting r derivatives,

$$\boldsymbol{L} = \begin{bmatrix} 0 & \mathrm{D}^* & \frac{\partial}{r\partial\theta} & \frac{\partial}{\partial z} & 0 \\ -\frac{\partial}{\partial r} & \nabla^2 - \frac{1}{r^2} & -\frac{2\partial}{r^2\partial\theta} & 0 & 0 \\ -\frac{\partial}{r\partial\theta} & \frac{2\partial}{r^2\partial\theta} & \nabla^2 - \frac{1}{r^2} & 0 & 0 \\ -\frac{\partial}{\partial z} & 0 & 0 & \nabla^2 & 0 \\ 0 & -T_c' & 0 & 0 & \nabla^2 \end{bmatrix}, \tag{7c}$$

$$\boldsymbol{M} = \begin{bmatrix} 0 & 0 & 0 & 0 & 0 \\ 0 & 0 & 0 & 0 & \frac{r_1 r_2}{r^2} \\ 0 & 0 & 0 & 0 & 0 \\ 0 & 0 & 0 & 0 & 0 \\ 0 & 0 & 0 & 0 & 0 \end{bmatrix}, \tag{7d}$$

and

$$N = \{0, 0, 0, 0, V \cdot \nabla\theta\}^T, \tag{7e}$$

Next, we introduce the expansions:

$$R_m = R^{(0)} + \epsilon R^{(1)} + \epsilon^2 R^{(2)} + \ldots, \tag{8a}$$

$$\boldsymbol{X} = \epsilon \boldsymbol{X}^{(1)} + \epsilon^2 \boldsymbol{X}^{(2)} + \epsilon^3 \boldsymbol{X}^{(3)} + \ldots, \tag{8b}$$

where ϵ is the small convection amplitude and we only consider terms up to $O(\epsilon^3)$ in this paper. At $O(\epsilon)$ we find:

$$(\boldsymbol{L} + R^{(0)} \boldsymbol{M}) \boldsymbol{X}^{(1)} = 0, \tag{9a}$$

with homogeneous boundary conditions $\{V_r, V_\Theta, V_z, \Theta\}^{(1)} = 0$ at r_1, r_2. The solution for $\boldsymbol{X}^{(1)}$ is of course that given in §3 suitably normalized, e.g. $\Theta^{(1)} = 1$ at $r = r_1$, and can be written in the form:

$$\boldsymbol{X}^{(1)} = \begin{bmatrix} p^{(1)}(r) & \cos n\theta & \cos kz \\ V_r^{(1)}(r) & \cos n\theta & \cos kz \\ V_\theta^{(1)}(r) & \sin n\theta & \cos kz \\ V_z^{(1)}(r) & \cos n\theta & \sin kz \\ \Theta^{(1)}(r) & \cos n\theta & \cos kz \end{bmatrix}, \tag{9b}$$

with $R^{(0)}$, n, and k being any of the critical states (bifurcation points) of stability surfaces similar to the one in figure 1.

At $O(\epsilon^2)$ we find:

$$(\boldsymbol{L} + R^{(0)} \boldsymbol{M}) \boldsymbol{X}^{(2)} = -R^{(1)} \boldsymbol{M} \boldsymbol{X}^{(1)} + N(\boldsymbol{X}^{(1)}, \boldsymbol{X}^{(1)}). \tag{10}$$

Solutions of the non-homogeneous system in (10) are only possible if the right-hand side is orthogonal to solutions of the adjoint homogeneous problem:

$$(\boldsymbol{L}^+ + R^{(0)} \boldsymbol{M}^+) \boldsymbol{X}^+ = 0. \tag{11a}$$

The adjoint operators $\boldsymbol{L}^+$ and $\boldsymbol{M}^+$ are given by:

$$\boldsymbol{L}^+ = \begin{bmatrix} 0 & \mathrm{D}^* & \frac{\partial}{r\partial\theta} & \frac{\partial}{\partial z} & 0 \\ -\frac{\partial}{\partial r} & \nabla^2 - \frac{1}{r^2} & -\frac{2\partial}{r^2 \partial\theta} & 0 & -T_c' \\ -\frac{\partial}{r\partial\theta} & \frac{2\partial}{r^2\partial\theta} & \nabla^2 - \frac{1}{r^2} & 0 & 0 \\ -\frac{\partial}{\partial z} & 0 & 0 & \nabla^2 & 0 \\ 0 & 0 & 0 & 0 & \nabla^2 \end{bmatrix}, \tag{11b}$$

$$\boldsymbol{M}^+ = \begin{bmatrix} 0 & 0 & 0 & 0 & 0 \\ 0 & 0 & 0 & 0 & 0 \\ 0 & 0 & 0 & 0 & 0 \\ 0 & 0 & 0 & 0 & 0 \\ 0 & \frac{r_1 r_2}{r^2} & 0 & 0 & 0 \end{bmatrix}, \tag{11c}$$

such that $(X^+, \boldsymbol{L}X) = (X, \boldsymbol{L}^+X^+)$ and $(X^+, \boldsymbol{M}X) = (X, \boldsymbol{M}^+X^+)$ with the inner product:

$$(X, Y) = \int_{r_1}^{r_2} r\,\mathrm{d}r \int_0^{\frac{2\pi}{n}} \mathrm{d}\theta \int_0^{\frac{2\pi}{k}} \mathrm{d}z\, X^T Y. \tag{11d}$$

Thus we find

$$X^+ = \begin{bmatrix} p^+(r) & \cos n\theta & \cos kz \\ V_r^+(r) & \cos n\theta & \cos kz \\ V_\theta^+(r) & \sin n\theta & \cos kz \\ V_z^+(r) & \cos n\theta & \sin kz \\ \Theta^+(r) & \cos n\theta & \cos kz \end{bmatrix}, \tag{11e}$$

with X^+ satisfying the same homogeneous conditions as $X^{(1)}$, and a normalization condition, e.g. $\Theta^{+\prime} = 1$ at $r = r_1$. Like $X^{(1)}$, X^+ is computed using Chebyshev pseudospectral solution of (11*a*).

With $X^{(1)}$ given by (9*b*), we evaluate the right-hand side of (10) as

$$\begin{aligned} &\Big\{0, -\frac{r_1 r_2}{r^2} R^{(1)}\Theta^{(1)} \cos n\theta \cos kz, 0, 0, \tfrac{1}{4}\Big[V_r^{(1)}\Theta^{(1)\prime} - \frac{n}{r}\Theta^{(1)} V_\theta^{(1)} - k\Theta^{(1)} V_z^{(1)}\Big] \\ &+\tfrac{1}{4}\cos 2n\theta\Big[V_r^{(1)}\Theta^{(1)\prime} + \frac{n}{r}\Theta^{(1)} V_\theta^{(1)} - k\Theta^{(1)} V_z^{(1)}\Big] + \tfrac{1}{4}\cos 2kz\Big[V_r^{(1)}\Theta^{(1)\prime} - \frac{n}{r}\Theta^{(1)} V_\theta^{(1)} \\ &+k\Theta^{(1)} V_z^{(1)}\Big] + \tfrac{1}{4}\cos 2n\theta \cos 2kz\Big[V_r^{(1)}\Theta^{(1)\prime} + \frac{n}{r}\Theta^{(1)} V_\theta^{(1)} + k\Theta^{(1)} V_z^{(1)}\Big]\Big\}^T. \end{aligned} \tag{12}$$

The compatibility condition that the inner product of (12) and X^+ should vanish leads to:

$$R^{(1)} = 0, \tag{13}$$

and thus bifurcation cannot be two-sided and is either supercritical or subcritical (Joseph 1976) depending on the sign of $R^{(2)}$ which is determined from compatibility at $O(\epsilon^3)$. Solution of (10) for $X^{(2)}$ with $\{V_r, V_\theta, V_z, \Theta\}^{(2)} = 0$ at r_1, r_2 is constructed by Chebyshev pseudospectral representation and is written in the form

$$X^{(2)} = \begin{bmatrix} p_0^{(2)}(r) + p_n^{(2)}(r)\cos 2n\theta + p_k^{(2)}(r)\cos 2kz + p_{nk}^{(2)}(r)\cos 2n\theta\cos 2kz \\ V_{r_0}^{(2)}(r) + V_{r_n}^{(2)}(r)\cos 2n\theta + V_{r_k}^{(2)}(r)\cos 2kz + V_{r_{nk}}^{(2)}(r)\cos 2n\theta\cos 2kz \\ V_{\theta_n}^{(2)}(r)\cos 2n\theta + V_{\theta_{nk}}^{(2)}(r)\cos 2n\theta\cos 2kz \\ V_{z_k}^{(2)}(r)\cos 2kz + V_{z_{nk}}^{(2)}(r)\cos 2n\theta\cos 2kz \\ \Theta_0^{(2)}(r) + \Theta_n^{(2)}(r)\cos 2n\theta + \Theta_k^{(2)}(r)\cos 2kz + \Theta_{nk}^{(2)}(r)\cos 2n\theta\cos 2kz \end{bmatrix}. \tag{14}$$

With $R^{(1)} = 0$ and $X^{(2)}$ given by (14) we find at $O(\epsilon^3)$

$$(\boldsymbol{L} + R^{(0)}\boldsymbol{M})X^{(3)} = -R^{(2)}\boldsymbol{M}X^{(1)} + N(X^{(1)}, X^{(2)}) + N(X^{(2)}, X^{(1)}), \tag{15}$$

and the right-hand side of (15) becomes

$$\begin{aligned} &\Big\{0, -\frac{r_1 r_2}{r^2} R^{(2)}\Theta^{(1)} \cos n\theta \cos kz, 0, 0, V_r^{(1)} \cos n\theta \cos kz \frac{\partial\Theta^{(2)}}{\partial r} \\ &+\frac{1}{r} V_\theta^{(1)} \sin n\theta \cos kz \frac{\partial\Theta^{(2)}}{\partial\theta} + V_z^{(1)} \cos n\theta \sin kz \frac{\partial\Theta^{(2)}}{\partial z} + \Theta^{(1)\prime} \cos n\theta \cos kz\, V_r^{(2)} \\ &-\frac{n}{r}\Theta^{(1)} \sin n\theta \cos kz V_\theta^{(2)} - k\Theta^{(1)} \cos n\theta \sin kz V_z^{(2)}\Big\}^T. \end{aligned} \tag{16}$$

n	k	From (19)	Numerical
3	0	6.237×10^{-4}	6.245×10^{-4}
4	0	7.650×10^{-4}	7.654×10^{-4}
5	0	7.257×10^{-4}	7.259×10^{-4}
0	3.1	6.658×10^{-4}	6.661×10^{-4}
3	2.04	4.789×10^{-4}	4.784×10^{-4}

TABLE 1. Slope of Nu–R_m lines at bifurcation. $r\theta$, rz, and $r\theta z$ numerical values are computed on uniform 40×40, 50×50, and $30 \times 30 \times 30$ meshes, respectively

The compatibility condition that the inner product of (16) and $\boldsymbol{X}^+$ should vanish leads to

$$R^{(2)} = \Big(\Theta^+, \Big\{ V_r^{(1)}(\Theta_0^{(2)'} + (\tfrac{1}{2}c_n\,\Theta_n^{(2)'} + (\tfrac{1}{2}c_k\,\Theta_k^{(2)'}) + \tfrac{1}{4}c_n\,c_k\,\Theta_{nk}^{(2)'}) - V_\theta^{(1)}\frac{n}{r}(\Theta_n^{(2)} + c_k\,\Theta_{nk}^{(2)}) - V_z^{(1)}\,k(\Theta_k^{(2)} + c_n\,\Theta_{nk}^{(2)}) + \Theta^{(1)'}(V_{r_0}^{(2)} + (\tfrac{1}{2}c_n\,V_{r_n}^{(2)} + \tfrac{1}{2}c_k\,V_{r_k}^{(2)}) + \tfrac{1}{4}c_n\,c_k\,V_{r_{nk}}^{(2)}) - \Theta^{(1)}\frac{n}{2r}(V_{\theta_n}^{(2)} + \tfrac{1}{2}c_k\,V_{\theta_{nk}}^{(2)}) - \Theta^{(1)}\tfrac{1}{2}k(V_{z_k}^{(2)} + \tfrac{1}{2}c_n\,V_{z_{nk}}^{(2)}) \Big\}\Big)/(V_r^+, r_1 r_2\,\Theta^{(1)}/r^2), \quad (17)$$

where $c_0 = 2$, and $c_m = 1$, $m \geqslant 1$. It is observed that the arbitrary normalizations of $\boldsymbol{X}^{(1)}$ and $\boldsymbol{X}^+$ have no influence on the sign of $R^{(2)}$. However, the normalization of $\boldsymbol{X}^{(1)}$ does influence the magnitude of $R^{(2)}$. Enhancement of heat transfer by convection, which is of primary interest in applications, is measured by the Nusselt number, Nu, which is the ratio of convective to diffusive transfer and is given by

$$Nu = 1 + \epsilon^2 c_n\,c_k \ln(\eta)\, r_j\,\Theta_0^{(2)'}(r_j) \quad (j = 1, 2). \quad (18)$$

Thus $r_j\,\Theta_0^{(2)'}(r_j)$, $j = 1, 2$ must be a constant which can be easily shown for two-dimensional bifurcations with either $n = 0$ or $k = 0$. This condition also served as a check on the numerical evaluations. As in the case of $R^{(2)}$, the value of Nu, for a given value of ϵ, is dependent on the normalization of $\boldsymbol{X}^{(1)}$, however the slope of the Nu–Ra line at bifurcation is not, and is given by

$$\frac{c_n\,c_k \ln(\eta)\, r_j\,\Theta_0^{(2)'}(r_j)}{R^{(2)}}. \quad (19)$$

The results of computations with $\eta = 0.46$ for the pair of two-dimensional bifurcations, and the critical three-dimensional motion, are given in table 1. It is found that $R^{(2)} > 0$ for the cases listed. Thus all bifurcations are supercritical. In addition, the critical three-dimensional motion is stable (Joseph, 1976). Table 1 lists the slopes of the Nu–Ra curves at bifurcation given by (19) and as found in the next section from numerical solutions of (3) and (4). The agreement is excellent and serves as a check on the computer code.

5. Direct numerical solutions

Sections 3 and 4 provide information at the onset of convection. In particular, with $\eta = 0.46$, a three-dimensional motion with $n = 3$ and $k = 2.04$ is predicted at $R_m = 1802.36$ as a stable supercritical bifurcation. The properties of this motion as the

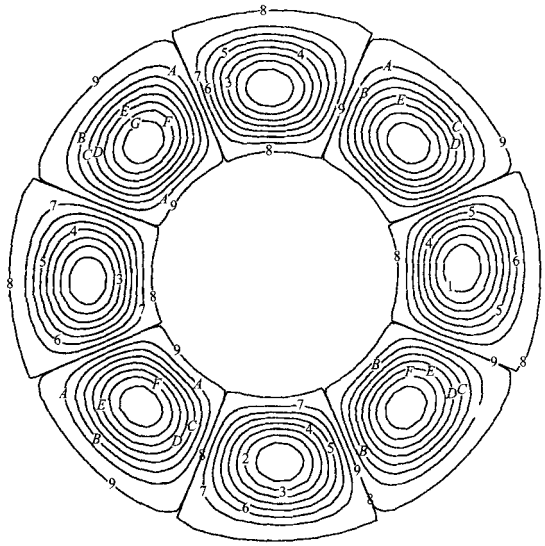

FIGURE 4. Streamlines of the two-dimensional $n = 4$, $k = 0$ azimuthal convection at $R_m = 2500$ produced on a 30×80 uniform mesh with initial condition (20). $\eta = 0.46$ and $Pr = 1$. There are 8 mirror-image vortices.

amplitude of convection ϵ increases can only be determined numerically. Thus in this section we only consider a finite cylindrical shell with periodicity conditions at $z = 0$ and $2\pi/k$. As R_m increases beyond the critical value, an azimuthal, two-dimensional motion with $n = 4$ becomes possible at $R_m = 1831.23$. At yet higher values of R_m these two distinct motions compete and the form of realizable convection can only be determined from computations with arbitrary initial conditions. We construct these numerical solutions by the finite volume procedure described by Bottaro & Zebib (1989). Briefly, the computational domain is divided into cylindrical cells with the grid points located at the geometric centres of these small cells. Additional boundary points are included to incorporate the boundary conditions. The discretized equations are obtained by integrating the conservation equations over the cells and assuming local linear variations in any of the primitive variables. Thus, our scheme is second-order accurate in space. Pressure–velocity coupling is as described in Patankar, 1980. Staggered location for the velocity components is adopted to avoid unrealistic pressure fields and associated numerical instabilities. Time marching toward steady states is accomplished by a fully implicit first-order forward Euler scheme. While the computer code has been previously verified, the full agreement with the asymptotic results of §4 provide yet additional verification for the numerics.

5.1. *Two-dimensional solutions*

Figure 4 is a plot of $n = 4$ and $k = 0$ azimuthal streamlines, the motion observed experimentally by Odenbach (1993) at $R_m = 2500$ and $Pr = 1$. This steady convection was initiated according to

$$V = 0, \quad T = T_c + \epsilon_1 \sin(\pi\theta/n) \sin(r - r_1), \tag{20}$$

with a small amplitude ϵ_1, typically $\leqslant 0.1$. It is immediately obvious that there are $2n$ mirror-image vortices. Thus all subsequent computations are performed in a wedge $r_1 \leqslant r \leqslant r_2, 0 \leqslant \theta \leqslant \pi/n$ with symmetry azimuthal boundary conditions. Solutions in such wedges corresponding to $n = 3$, 4, 5 (the corresponding critical R_m, respectively,

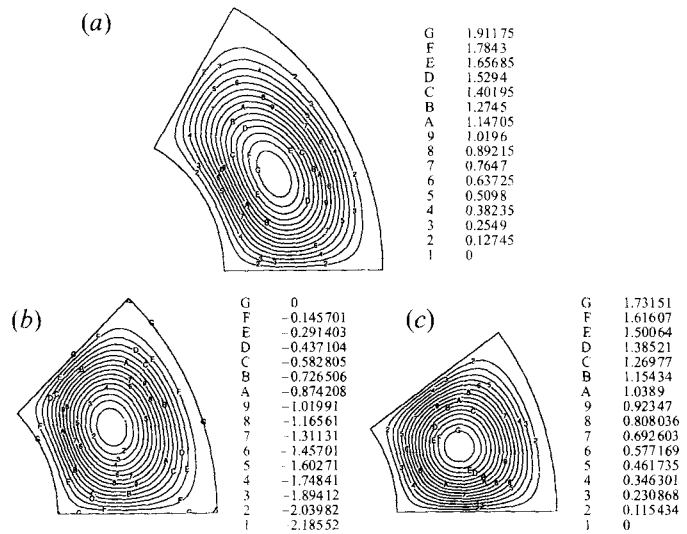

FIGURE 5. Streamlines similar to a single vortex of figure 4 produced on a 40×40 uniform mesh and with (*a*) $n = 3$, (*b*) 4 and (*c*) 5, $Pr = 1$, $\eta = 0.46$, and $R_m = 2500$. The motion is fastest with $n = 4$ as expected.

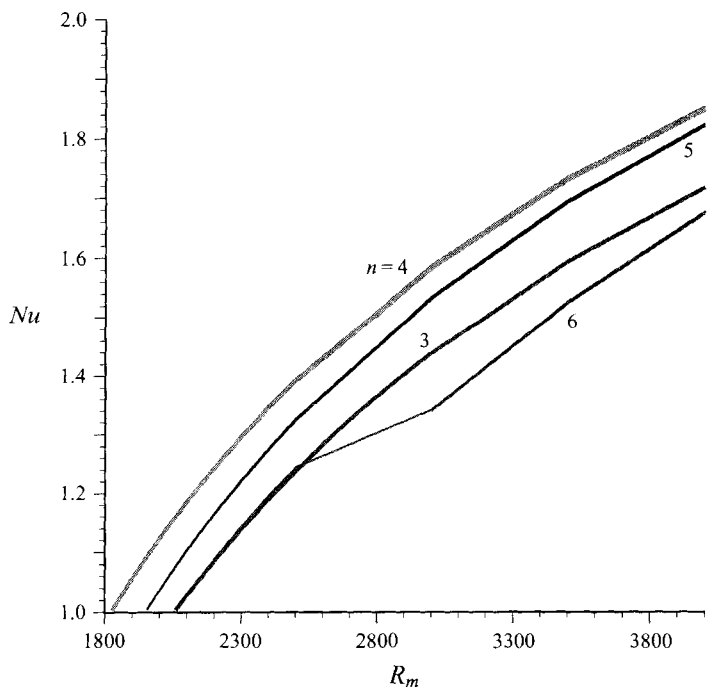

FIGURE 6. Nusselt numbers for different two-dimensional azimuthal motions computed on different wedges similar to those in figure 5. Each curve represents three values of Pr: 1, 10 and 100. The values are so close that a single line appears on this scale. A large change in R_m can produce motions with $2n$ wedges as happened with $n = 3$. Note that the branch with $n = 6$ can be continued down to $R_m = 2334$ which is the corresponding critical value.

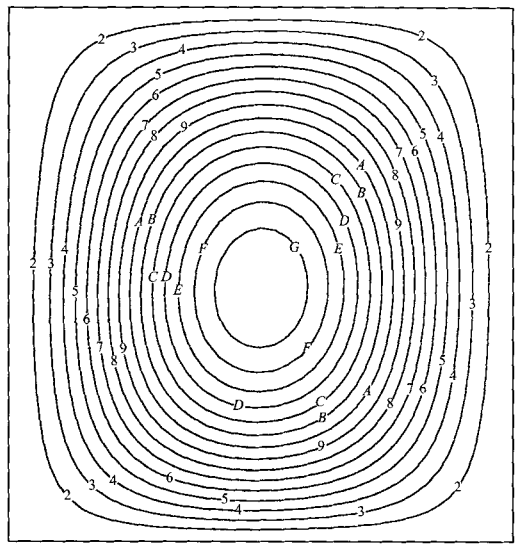

FIGURE 7. Meridional motion with $k = 3.1$, $Pr = \infty$, $\eta = 0.46$, and $R_m = 2500$, produced on a 40×40 uniform mesh.

are 2063.75, 1831.23, and 1956.62), $R_m = 2500$, and $Pr = 1$ are shown in figure 5. These solutions were produced on a uniform 40×40 mesh. The negligible influence of Prandtl numbers $\geqslant 1$ on convection is seen from the resulting Nu–Ra plots shown in figure 6. Thus subsequent results are for infinite Pr which is computationally less expensive.

Likewise, meridional solutions in $r_1 \leqslant r \leqslant r_2$ and $0 \leqslant z \leqslant \pi/k$ are produced with initial conditions of the form

$$V = 0, \quad T = T_c + \epsilon_1 \sin(\pi z/k) \sin(r - r_1). \tag{21}$$

Streamlines produced on a 40×40 uniform mesh, with $k = 3.1$, $n = 0$, $R_m = 2500$, and $Pr = \infty$, are shown in figure 7.

5.2. *Three-dimensional solutions*

Three-dimensional solutions are produced in the wedge $r_1 \leqslant r \leqslant r_2, 0 \leqslant \theta \leqslant \pi/n$ and $0 \leqslant z \leqslant \pi/k$ with initial conditions of the form

$$V = 0, \quad T = T_c + \epsilon_1 \sin(\pi z/k) \sin(\pi\theta/n) \sin(r - r_1). \tag{22}$$

Figure 8 shows the Nu–R_m plots produced from computations with 20^3, 24^3 and 26^3 uniform meshes. The resulting motion, computed on the 26^3 uniform mesh, can be visualized from isothermal-surface plots like the one shown in figure 9 with $R_m = 2500$ and $Pr = \infty$ from which the fluid velocity can be deduced by observing that it 'pushes' the isotherms.

Nusselt numbers of the three convective patterns for values of R_m just beyond onset are shown in figure 10. As expected, first a three-dimensional motion occurs, followed by azimuthal convection, and later meridional motion is also possible. For these weakly nonlinear states the dependence of Nu on R_m is almost linear with slopes in perfect agreement with the asymptotic results in table 1, as mentioned earlier. It is clear from figure 10 that azimuthal convection becomes more efficient in heat transfer than the three-dimensional motion for $R_m \geqslant 1890$. Thus, one has to consider the possibility that azimuthal convection may become the stable and preferred form of convection at higher R_m in agreement with the maximum heat transport hypothesis of Malkus (1954).

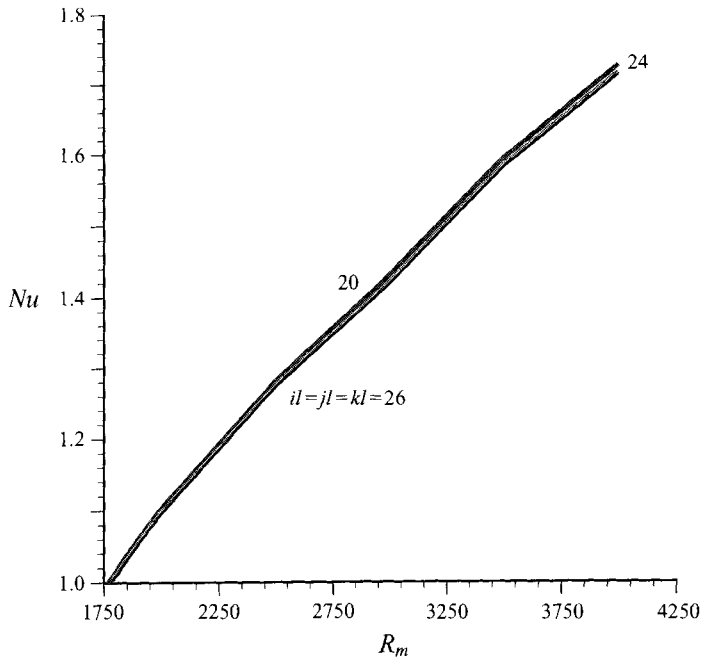

FIGURE 8. Nusselt numbers of preferred three-dimensional convection with $n = 3$, $k = 2.04$, $Pr = \infty$, and $\eta = 0.46$ computed on three uniform meshes. As in all results in this paper, the critical R_m obtained from nonlinear computations increases as the mesh is refined with the limiting value as obtained from linear theory. A 26^3 mesh is adequate for the range of R_m indicated.

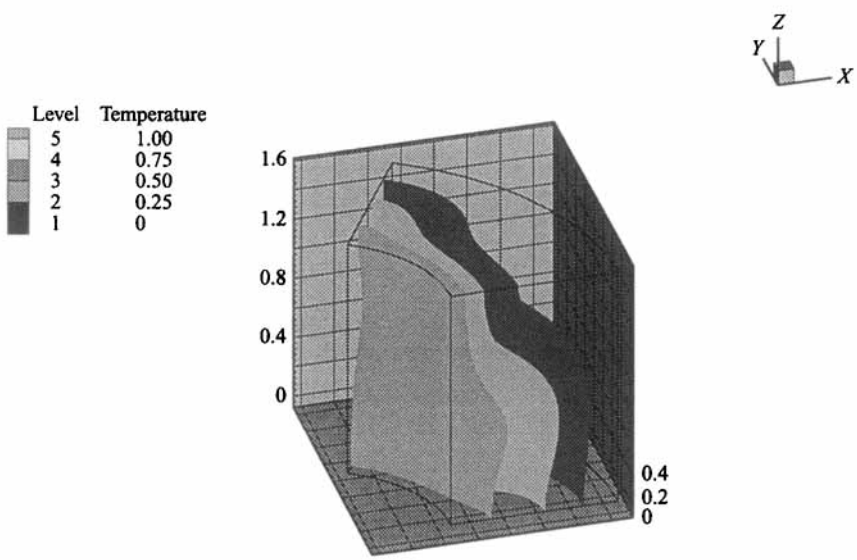

FIGURE 9. Isothermal surfaces of the $R_m = 2500$ convection of figure 8 on a 26^3 mesh. The sense of motion can be visualized as the fluid motion tends to 'push' the isotherms (counterclockwise in the (x, z)-plane and clockwise in the top (x, y)-plane). As in figures 4, 5 and 7, the motion can be reversed to produce a companion mirror image.

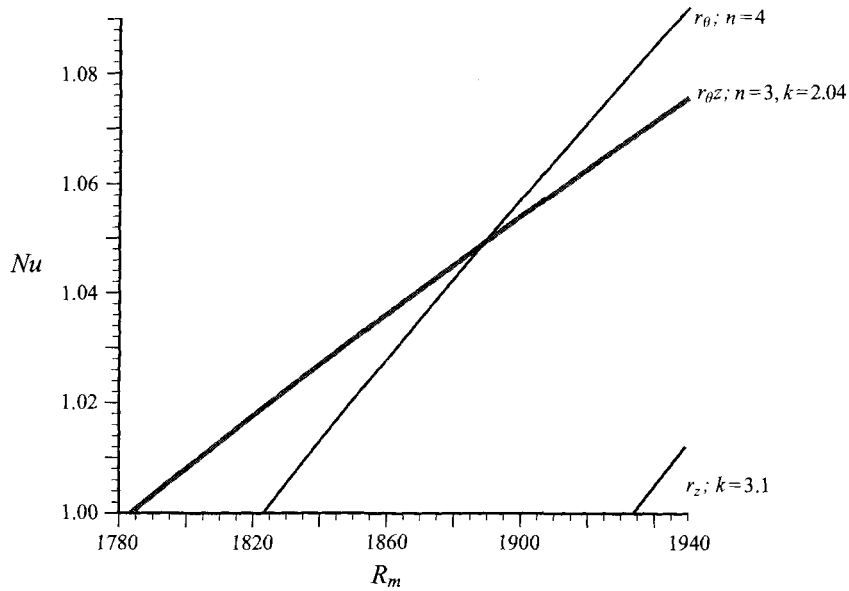

FIGURE 10. Nu–R_m lines at bifurcation of the $n = 3$ and $k = 2.04$ three-dimensional, $n = 4$ azimuthal, and $k = 3.1$ meridional states, produced with 26^3, 40^2, and 40^2 meshes, respectively. The slopes of these lines (with slightly finer meshes) at onset of convection are listed in table 1 and are in excellent agreement with those obtained from the asymptotic value (19).

R_m	Initial conditions, ϵ_1 and ϵ_2 are defined in (23)	Final state
1820	$\epsilon_1 = 0.1$	$n = 3; k = 2.04$; 3D
	$\epsilon_1 = \epsilon_2 = 0.1$	$n = 3; k = 2.04$; 3D
1850	$\epsilon_1 = 0.1$	$n = 3; k = 2.04$; 3D
	$\epsilon_1 = \epsilon_2 = 0.1$	$n = 3; k = 2.04$; 3D
1875	$\epsilon_1 = \epsilon_2 = 0.1$	$n = 3; k = 2.04$; 3D
1900	$\epsilon_1 = \epsilon_2 = 0.1$	$n = 3; k = 2.04$; 3D
1925	$\epsilon_1 = \epsilon_2 = 0.1$	$n = 4$; 2D
1950	$\epsilon_1 = 0.1$	$n = 4$; 2D
	$\epsilon_1 = \epsilon_2 = 0.1$	$n = 4$; 2D
2000	$\epsilon_1 = \epsilon_2 = 0.0$	$n = 4$; 2D
	$\epsilon_1 = \epsilon_2 = 0.1$	$n = 4$; 2D

TABLE 2. Stability using three-dimensional calculations on a $20 \times 20 \times 108$ $r_\theta z$ uniform mesh

5.3. *Stability of nonlinear states*

We determine the form of stable convection from calculations with initial conditions having contributions from competing states. These are of the form

$$V = 0, \quad T = T_c + \left[\epsilon_1 \sin\frac{\pi z}{k_1} \sin\frac{\pi\theta}{n_1} + \epsilon_2 \sin\frac{\pi\theta}{n_2}\right] \sin(r - r_1), \tag{23}$$

with $n_1 = 3$, $k_1 = 2.04$, and $n_2 = 4$. Computations are performed in the cylindrical shell $r_1 \leqslant r \leqslant r_2, 0 \leqslant \theta \leqslant 2\pi$ and $0 \leqslant z \leqslant \pi/k_1$ and thus both three-dimensional and

azimuthal convection are realizable. A $20 \times 20 \times 108$ mesh was used for computational economy and the results are given in table 2. For values of $R_m \geqslant 1925$ the results are conclusive. With various combinations of ϵ_1 and ϵ_2 either 0 or 0.1, the finaly steady state is $n = 4$ azimuthal convection in apparent agreement with experiments. For values of $R_m \leqslant 1875$ we conclusively recover steady three-dimensional solutions from a variety of initial conditions. The case $R_m = 1900$ required an extremely large number of iterations with the final steady state being three-dimensional. This then appears to be very close to the R_m value at transition to stable two-dimensional $n = 4$ states, and compares favourably with the value at transition to the state of higher heat transport ($R_m = 1890$) deduced from figure 10 with different truncation errors associated with different meshes.

6. Concluding remarks

We have considered thermal convection in a magnetic fluid. The particular impressed magnetic field was such that a radial body force field exists. This led to a potentially unstable situation in the presence of a radial temperature gradient. Linear, nonlinear, and computational techniques were used to study the phenomena. The results produced are in agreement with available experimental observation. Further quantitative comparison with experiments is desirable and there is need for additional experiments. Modification of the theory with allowance for a perturbed magnetic field can also be performed if necessary. There appears to be a great potential for engineering applications of magnetic fluids in microgravity. Furthermore, and from a fundamental viewpoint, the possibility of producing a magnetic field with a resulting central body force is exciting. Experiments on thermal instabilities in spherical shells with applications to mantle convection would be possible and verification of existing theories (Busse & Riahi 1982; Zebib 1993) can be pursued.

REFERENCES

BASHTOVOY, V. G., BERKOVSKY, B. M. & VISLOVICH, A. N. 1988 *Introduction to Thermomechanics of Magnetic Fluids*. Hemisphere.

BERKOVSKY, B. M., VEDVEDEV, V. F. & KRAKOV, M. S. 1993 *Magnetic Fluids Engineering Applications*. Oxford University Press.

BOTTARO, A. & ZEBIB, A. 1989 Three-dimensional thermal convection in Czochralski melt. *J. Crystal Growth* **97**, 50–58.

BUSSE, F. H. & RIAHI, N. 1982 Patterns of convection in spherical shells. Part 2. *J. Fluid Mech.* **123**, 283–301.

CHANDRASEKHAR, S. 1961 *Hydrodynamic and Hydromagnetic Stability*. Oxford University Press.

FINLAYSON, B. A. 1970 Convective instability of ferromagnetic fluids. *J. Fluid Mech.* **40**, 753–756.

GOTTLIEB, D. & ORSZAG, S. A. 1977 *Numerical Analysis of Spectral Methods: Theory and Applications*. Society of Industrial and Applied Mathematics.

JOSEPH, D. D. 1976 *Stability of Fluid Motions I*. Springer.

MALKUS, W. V. R. 1954 The heat transport and spectrum of thermal turbulence. *Proc. R. Soc. Lond.* A **225**, 196–212.

ODENBACH, S. 1993 Drop tower experiments on thermomagnetic convection. *Microgravity Sci. Tech.* **6**(3), 161–163.

PATANKAR, S. 1980 *Numerical Heat Transfer and Fluid Flow*. McGraw Hill.

POLEVIKOV, V. K. & FERTMAN, V. E. 1977 Investigation of heat transfer through a horizontal layer of a magnetic liquid for the cooling of cylindrical conductors with a current. *Magnetohydrodynamics* **13**, 11–16.

ROSENSWEIG, R. E. 1985 *Ferrohydrodynamics*. Cambridge University Press.

ROSENSWEIG, R. E. 1987 Magnetic Fluids. *Ann. Rev. Fluid Mech.*

SCHLÜTER, A., LORTZ, D. & BUSSE, F. 1965 On the stability of steady finite amplitude convection. *J. Fluid Mech.* **23**, 129–144.

STILES, P. J. & BLENNERHASSETT, P. J. 1993 Stability of cylindrical Couette flow of a radially magnetized ferrofluid in a radial temperature gradient. *J. Magnetism Mag. Mat.* **122**, 207–209.

ZEBIB, A. 1993 Linear and weakly-nonlinear variable viscosity convection in spherical shells. *Theoret. Comput. Fluid Dyn.* **4**, 241–253.